THE JOURNAL OF PHYSICAL CHEMISTRY C
A JOURNAL OF THE AMERICAN CHEMICAL SOCIETY

pubs.acs.org/JPCC

Article

Controllable Electrochemical Deposition and Theoretical Understanding of Conformal Perovskite on Textured Silicon towards Efficient Perovskite/Silicon Tandem Solar Cells

Yangrunqian Wang, Chao Gao, Xin Wang, Hong Liu, and Wenzhong Shen*

Cite This: J. Phys. Chem. C 2021, 125, 2875−2883

Read Online

ACCESS | Metrics & More | Article Recommendations

ABSTRACT: Perovskite (PSK)/crystalline silicon (c-Si) monolithic tandem solar cells (TSCs) are considered as a promising alternative to break the single-junction Shockley−Queisser efficiency limit. However, existing methods for preparing PSK on textured c-Si solar cells are either technically complex or expensive. Here, we report a simple and efficient two-step electrochemical deposition method for the conformal growth of nanoscale PSK on traditional pyramid-shaped textured silicon heterojunction solar cells. In combination with the simulation based on the Butler−Volmer model, we have understood the electrode dynamics of the overpotential deposition of uniform Pb on the textured silicon surface, followed by the complete conversion of the deposited Pb into conformal and nanoscale PSK. The nucleation and growth of Pb and PSK can be conveniently optimized by adjusting the bias voltage, and the entire electrochemical deposition process can be completed in a few minutes. We have further investigated theoretically the effect of the pyramid height and angle on the uniformity and thickness distribution of the Pb deposition and PSK conversion. The present work establishes an easy way for low-cost PSK/c-Si monolithic TSCs.

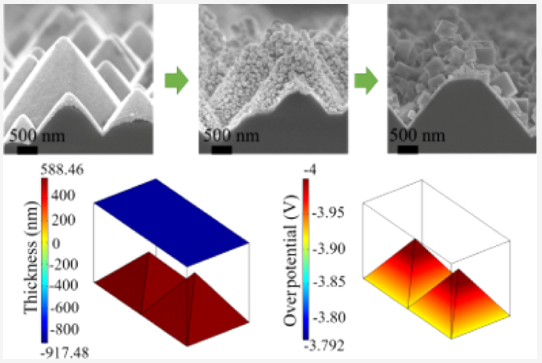

INTRODUCTION

Crystalline silicon (c-Si) solar cells dominate the photovoltaic market (over 90%[1]), and their power conversion efficiency (PCE) has reached a world record of 26.7%.[2] It is very close to the Shockley−Queisser efficiency limit of 29.4%[3] and leaves little room for improvement. Perovskite (PSK)/c-Si monolithic tandem solar cells (TSCs) are considered as a promising alternative to break the limit by achieving spectral distributed absorption. The PSK solar cell serves as the top subcell and has an adjustable band gap of 1.5−2.3 eV. A c-Si solar cell with a band gap of 1.12 eV is the bottom subcell. Theoretically, the optimal efficiency of a double-junction cell with full spectral matching can be as high as 43%,[4] predicting the enormous potential.

Over the past 5 years, the PCEs for PSK/c-Si monolithic TSCs have increased significantly from the original 13.7%[5] to the recently certified 29.5%.[2] Limited to the PSK preparation methods only for flat substrates, early research studies were done on c-Si solar cells with front-polished surfaces.[5−8] Mailoa et al.[5] drew on proven $MAPbI_3$ (MA = CH_3NH_3) PSK technology and reported 13.7% PCE in 2015. Nearly at the same time, Albrecht et al.[6] realized a higher efficiency of 18.1% using $FAMAPbI_{3-X}Br_X$ [FA = $HC(NH_2)_2$] for a better matched spectrum. Later that year, indium zinc oxide (IZO) was used to replace indium tin oxide (ITO) as the charge-carrier recombination layer because of better energy level matching and the efficiency was raised to 21.2%.[7] In 2017, the McGehee group[8] achieved a certification efficiency of 23.6%. They used $CsFAPbI_{3-X}Br_X$ as the absorption layer instead and modified c-Si with Si nanoparticles on the rear, which optimizes the light absorption. Nevertheless, c-Si solar cells with front-polished surfaces are actually not ideal for bottom subcells because of their severe light absorption losses.[9]

To tackle the conformal growth of PSK on pyramid-shaped textured c-Si solar cells, many attempts have been made recently on the shape-preserving growth of PSK materials. The growth methods of conformal PSK layers can be divided into four aspects: (1) solution route;[10] (2) dual-source co-evaporation method;[11] (3) blade-coating process;[12] and (4) mechanically stacking.[13] In the first case, the PCE was increased to 25.7% by using a higher concentration (1.65−1.75 M) of PSK precursors to prepare micron PSK layers on the pyramid-shaped textured c-Si solar cells.[10] To overcome

Received: December 18, 2020
Revised: January 19, 2021
Published: February 2, 2021

https://dx.doi.org/10.1021/acs.jpcc.0c11259
J. Phys. Chem. C 2021, 125, 2875−2883

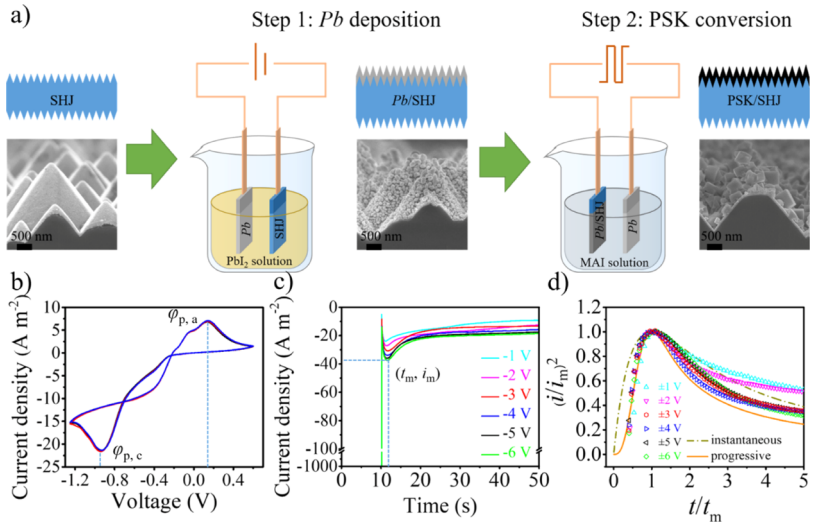

Figure 1. (a) Schematic illustration of the two-step electrodeposition of PSK thin films on SHJ solar cells, together with the corresponding cross-sectional SEM images. (b) Cyclic voltammetry curves of Pb measured in the PbI_2 solution. (c) Experimental current−time transient curves at different potentials. (d) Experimental (boxes) and theoretical (curves) dimensionless $(i/i_m)^2$ vs (t/t_m) data for instantaneous and progressive nucleation of Pb at different potentials.

the resulting electrical degradation, they deposited a self-limiting passivation layer on the surface of the PSK. It tripled the depletion width at the pyramid valley and inhibited phase segregation. Although the micron PSK is the simplest and most direct method, it results in a flat front surface after PSK deposition, which still causes light absorption loss. In the second case, the conformal growth of nanoscale PSK on pyramid-shaped textured c-Si solar cells was realized by combining the dual-source co-evaporation and solution path by Sahli et al.[11] They prepared the PSK layer by co-evaporating CsBr and PbI_2 powders before spin-coating FABr and FAI. The spin-coated solutions penetrated into the CsBr and PbI_2 scaffolds, converting them into nanoscale PSK films and realizing the conformal growth on the pyramid-shaped textured c-Si solar cells. The PCE was raised to 25.2%. However, during the evaporation, toxic lead gas was produced, and the preparation is complex. For the third case, Chen et al.[12] introduced a nitrogen-assisted scraper process to deposit micron PSK to completely cover the pyramid-shaped textured c-Si solar cells. They applied polydimethylsiloxane (PDMS) as the light-scattering layer on the top of the PSC to reduce the reflectivity and achieved a PCE of 26%. The disadvantage is that this method still leaves the same flat front surface as in the first case, leading to inevitable absorption losses. For the fourth case, Lamanna et al.[13] proposed a mechanically stacked PSK/c-Si scheme, where the rear electrode of the PSK top cell is bonding with the front metal grid of the textured c-Si bottom cell. They raised the PCE to 26.3% by further optimizing the functional layers to minimize the optical and electrical losses. The disadvantages are the optical loss caused by the silver metal finger bonding and the increase of manufacturing costs.

Our goal is to find an effective and simple way to realize the conformal growth of nanoscale PSK layers that fully cover the pyramid-shaped textured c-Si solar cells. The present novel idea comes from the exploration of electrodeposition of Pb on n-Si (111)[14] and the electrochemical formation of Pb oxides to react with MA^+ for PSK deposition.[15−17] We have realized the two-step electrochemical deposition of PSK solar cells on FTO glasses.[18] In this paper, we report on the successful electrochemical deposition of nanoscale and conformal $MAPbI_3$ PSK growth on the traditional pyramid-shaped textured silicon heterojunction (SHJ) solar cells with naturally the surface ITO-conducting layer.[1,19] The grain sizes and thickness of Pb and PSK can be conveniently optimized by adjusting the bias voltage, and the entire electrochemical deposition process can be completed in a few minutes. Furthermore, the electrochemical deposition process has been well understood based on the Butler−Volmer model[20−24] to clearly reveal the related principles of electrode dynamics. We have further investigated theoretically the effect of the pyramid height and angle on the lead and PSK deposition for guidance of the subsequent research on PSK/c-Si TSCs.

METHODS

Preparation of Electrolytes. In step 1, 0.13 mol sodium iodide (NaI, Aladdin reagent, 99.99%) was dissolved into 100 mL of isopropanol (Sinopharm Chemical Reagent Co., Ltd, 99%). The mixture was stirred at 45 °C for 2 h and then filtered to obtain the clear solution. 1 mmol PbI_2 (Sigma-Aldrich, 99.99%) was dissolved into 100 mL of the as-prepared solution and stirred until clear. In step 2, 1 g of MAI (Xi'an Polymer Light Technology Corp, 99%) was dissolved into 100 mL of isopropanol and stirred until clear. Both electrolytes were refiltered before used.

Preparation of Substrates. Factory-made 156 × 156 mm^2 traditional SHJ solar cells[25] were cut into small pieces of 2 × 2 cm^2. The as-made 2 × 2 cm^2 SHJ solar cells were cleaned sequentially via detergent, DI water, acetone, isopropanol, and ethanol under ultrasonication for 15 min and dried with N_2 flow.

Two-Step Electrochemical Deposition. In step 1 of the Pb deposition, the bias voltage was set from −1 to −6 V and the deposition time was 300 s. After deposition, the resultant film was rinsed with isopropanol and then dried with N_2 flow. In step 2 of the PSK conversion, the symmetric square-wave pulse voltage was set at the positive pulse voltage for 100 ms and then at the negative pulse voltage for 100 ms in one cycle. The amplitude was set at 1−6 V and the conversion time was

https://dx.doi.org/10.1021/acs.jpcc.0c11259
J. Phys. Chem. C 2021, 125, 2875−2883

400 s. After deposition, the resultant film was rinsed with isopropanol and then dried with N_2 flow.

Characterization. The cyclic voltammetry measurement and electrochemical deposition were conducted on the electrochemical workstation (Vertex. C. EIS, Ivium, Netherlands). The morphology of the samples was observed by a field-emission scanning electron microscope (Zeiss Ultra Plus, Germany). The structural information was examined via an X-ray diffractometer (D8 ADVANCE Da Vinci, Bruker, Germany). The absorption spectra were measured by the UV−vis−NIR spectrophotometer (LAMDA950, PerkinElmer, USA). The steady-state photoluminescence (PL) and time-resolved PL (TRPL) of the samples were measured by a fluorescence spectrometer (QM/TM/IM, PTI, USA) with an excitation wavelength of 510 nm.

RESULTS AND DISCUSSION

Electrochemical Deposition of Pb on SHJ Solar Cells. To realize the shape-preserving growth of nanoscale $MAPbI_3$ PSK on pyramid-shaped textured SHJ solar cells, we introduce a two-step electrochemical deposition method. The precursor (i.e., Pb) is first deposited before converting into PSK. The process is illustrated in Figure 1a. For preparation, we cut the factory-made 156 × 156 mm^2 SHJ solar cells into small pieces of 2 × 2 cm^2. Then, we cleaned the as-made 2 × 2 cm^2 SHJ solar cells sequentially via detergent, DI water, acetone, isopropanol, and ethanol under ultrasonication for 15 min and dried the SHJ solar cells with N_2 flow for the next step. The cross-sectional SEM image in Figure 1a shows that the heights of pyramids of the SHJ solar cells are about several micrometers, which means that traditional spin-coating methods[26−30] of PSK preparation are not applicable for the factory-made pyramid-shaped textured SHJ solar cells. That is why we propose electrochemical deposition as a viable solution in this article.

For the electrochemical deposition, we used the classic two-electrode system.[18,31] As illustrated in Figure 1a, in step 1, we used a 2 × 2 cm^2 lead foil as the anode, the as-made 2 × 2 cm^2 SHJ solar cell as the cathode, and PbI_2−NaI mixed isopropanol solution as the electrolyte. Further details can be found in the Preparation of Electrolytes Section. NaI in the solution can provide I^- ions to assist the dissolution of PbI_2 in the isopropanol.[32] By applying a constant bias voltage, we successfully deposited Pb on the pyramid-shaped textured SHJ solar cells. From the cross-sectional SEM image, we can tell that the Pb grains are uniformly deposited on the pyramid-shaped textured SHJ solar cells, which is very important for converting them into conformal and nanoscale PSK in the next step. In step 2, on the contrary, we employed the prepared sample as the anode, the lead foil as the cathode, and MAI isopropanol solution as the electrolyte. We applied a manipulated bias voltage to convert the deposited Pb into PSK on the pyramid-shaped textured SHJ solar cells. As we can see, the cross-sectional SEM image shows that the nanoscale and conformal PSK is fully covered on pyramid-shaped textured SHJ solar cells, which proves that the electrochemical deposition method we bring up here is achievable and efficient.

We have taken a further look into the electrode dynamics of the electrochemical deposition process. In step 1, the reactions at the cathode are as follows[18]

$$Pb^{2+} + 2e^- \rightarrow Pb \quad (1)$$

$$2H^+ + 2e^- \rightarrow H^2 \quad (2)$$

while the reaction at the anode is

$$Pb \rightarrow Pb^{2+} + 2e^- \quad (3)$$

In order to locate the reduction and oxidation potentials corresponding to eqs 1 and 3, we conducted the cyclic voltammetry measurement.[33] We set the potential range from −1.25 to +0.65 V with a scan speed of 100 mV/s for three cycles. From the cyclic voltammetry curves in Figure 1b, we can learn that the reduction potential is at ∼ −0.94 V and the oxidation potential is at ∼ +0.14 V, corresponding to $\varphi_{p,c}$ and $\varphi_{p,a}$, respectively. Generally, there are two kinds of electrochemical deposition for metals, overpotential deposition (OPD) and underpotential deposition (UPD).[14,34] OPD means that the applied bias voltage is higher than the reduction potential, which can induce a three-dimensional (3D) continuous growth, leading to a uniform polycrystalline layer.[34] In contrast, when the applied bias voltage is lower than the reduction potential, the UPD case only results in a single monoatomic or subatomic layer.[34] In the following process, we therefore set the applied bias voltage higher than −0.94 V for the OPD of Pb to happen. As shown in Figure 1c, when we applied a bias voltage of −1−−6 V on SHJ solar cells, we can find out that there are two stages in all the cases. At the first stage, the voltage decreases very sharply, corresponding to the area near the left vertical axis. This is because of the double layer charging and the necessary decay for triggering the OPD of Pb.[35] At the second stage, after the sharp decrease, the current increases to the maximum (i_m) at time (t_m) and then decreases to a certain value gradually. These two stages indicate the nucleation and growth processes of Pb on the SHJ solar cells, respectively.[34,36] We need to point out that in spite of the different bias voltages, all the curves in Figure 1c include those two stages, which means that the nucleation and growth processes of Pb on the SHJ solar cells can happen at all the different voltages.

As we know, there are two extreme situations in the electrochemistry nucleation process:[34] the instantaneous and progressive nucleation. In instantaneous nucleation, all the activation points turn into nucleation points at the very beginning ($t = 0$). Afterward ($t > 0$), there are no more newly generated nucleation points. While in the case of progressive nucleation, there are continuously generated nucleation points after the process begins ($t > 0$). The dimensionless functions of instantaneous and progressive nucleation are given below[34,36]

$$\left(\frac{i}{i_m}\right)^2 = \frac{1.9542}{t/t_m}\left\{1 - \exp\left[-1.2564\left(\frac{t}{t_m}\right)\right]\right\}^2 \quad (4)$$

$$\left(\frac{i}{i_m}\right)^2 = \frac{1.2254}{t/t_m}\left\{1 - \exp\left[-2.3367\left(\frac{t}{t_m}\right)\right]\right\}^2 \quad (5)$$

The experimental dimensionless $(i/i_m)^2$ vs (t/t_m) data represented by the boxes in Figure 1d are obtained from Figure 1c under the bias voltages of −1−−6 V. The dashed and solid curves in Figure 1d are in accordance with eqs 4 and 5 and the dimensionless functions of instantaneous and progressive nucleation, respectively. We can find out that when t/t_m is less than one, the boxes are well matched with the solid curve. It means that in this period, progressive nucleation is happening no matter the potentials. New nucleation points

https://dx.doi.org/10.1021/acs.jpcc.0c11259
J. Phys. Chem. C 2021, 125, 2875−2883

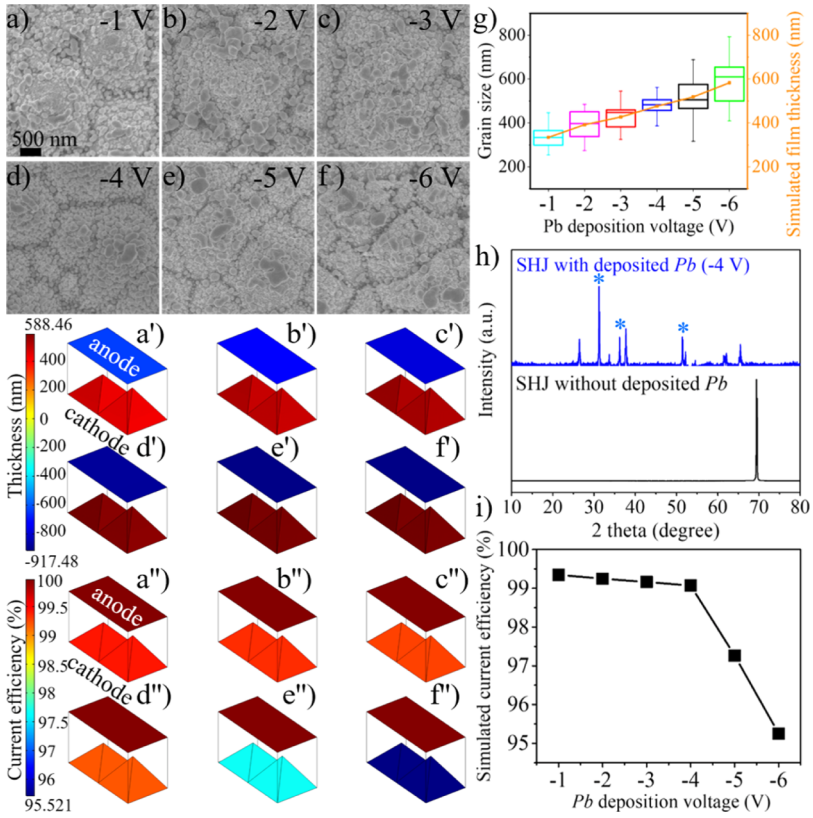

Figure 2. Top-view SEM images of the as-deposited Pb on SHJ solar cells at the potential of (a) −1, (b) −2, (c) −3, (d) −4, (e) −5, and (f) −6 V. (g) Statistics of the Pb grain size and the simulated film thickness at different potentials. (h) XRD patterns of SHJ solar cells without and with Pb deposited at −4 V potential. Illustrations of the simulated film thickness distribution of Pb on SHJ solar cells at the potential of (a′) −1, (b′) −2, (c′) −3, (d′) −4, (e′) −5, and (f′) −6 V. Illustrations of the simulated current efficiency at the potential of (a″) −1, (b″) −2, (c″) −3, (d″) −4, (e″) −5, and (f″) −6 V. (i) Simulated cathode current efficiency curve at different potentials.

keep generating and growing simultaneously. However, when t/t_m is more than one, the boxes depart from the solid curve, especially in the cases of the bias voltages of −1 V and −2 V. This indicates that in this period, the generation of new nucleation points is slowed down because Pb grains already covered the surface of the SHJ solar cells and leave less space for it. In conclusion, we find out that when we applied a voltage higher than the reduction potential of ∼ −0.94 V, there is a 3D progressive OPD on the SHJ solar cells. It allows us to simulate this process based on the Butler−Volmer model[20−24] by the software Multiphysics to further reveal the mechanism of lead OPD.

Figure 2a−f shows the top-view SEM images of the as-deposited Pb on pyramid-shaped textured SHJ solar cells at the bias voltage of −1−−6 V, respectively. From the images, we can find out that when the bias voltage is lower than −2 V, the coverage is not satisfied due to fewer nucleation points. With the bias voltage increasing, the coverage becomes uniform. However, when the bias voltage is higher than −5 V, because of many observable bubbles generated at the surface of the SHJ solar cells during the electrochemical deposition process, the uniform coverage is damaged. From eq 2, we can know that the bubbles are hydrogen as the byproduct. We have also illustrated in Figure 2g the statistics of Pb grain sizes. Although the average grain size is becoming higher with the increase of the bias voltage, the size distribution is more dispersed. To further confirm the existence of Pb on SHJ solar cells, we conducted the X-ray diffraction (XRD) measurement. The patterns of SHJ solar cells without and with Pb deposited at −4 V potential are shown in Figure 2h. We can see that there is a strong peak at 69.3° in the pattern of SHJ solar cells without deposited Pb, corresponding to the [100] lattice planes of the crystalline silicon.[37] When it comes to the pattern of SHJ solar cells with Pb deposited at −4 V potential, this strong peak disappears. That is because SHJ solar cells are covered with Pb grains and the X-ray cannot reach the crystalline silicon anymore.[38] Moreover, there are new peaks highlighted with "*" at 31.4, 36.4, and 52.6°, which are assigned to the [111], [200], and [220] crystal planes of lead, corresponding to the data from JCPDS card no. 6-0686.[18] The other peaks are assigned to ITO, as the transparent conducting oxides (TCO) on the surface of the pyramid-shaped textured SHJ solar cells,[1,19] which can also be found in the patterns of the converted PSK on the pyramid-shaped textured SHJ solar cells.

Simulation of the Electrochemical Deposition Process. Now, we simulate the electrochemical deposition process of Pb based on the Butler−Volmer model[20−24] by the software Multiphysics. In our case, given the fact that the distance between the two electrodes is ∼5 cm, which is many orders of magnitude higher than the thickness of the Pb layer (several hundred nanometers), the electroplating module is feasible.[22] Furthermore, the thicknesses of the SHJ solar cells and lead foil are ∼160 μm and 7 mm, respectively. They are also many orders of magnitude higher than the thickness of the Pb layer. Hence, in this process, we can use the secondary current distribution (SCD) model[22] of the electroplating module to simulate the electrochemical deposition process of Pb because the change of thickness is negligible compared to the thickness

https://dx.doi.org/10.1021/acs.jpcc.0c11259
J. Phys. Chem. C 2021, 125, 2875−2883

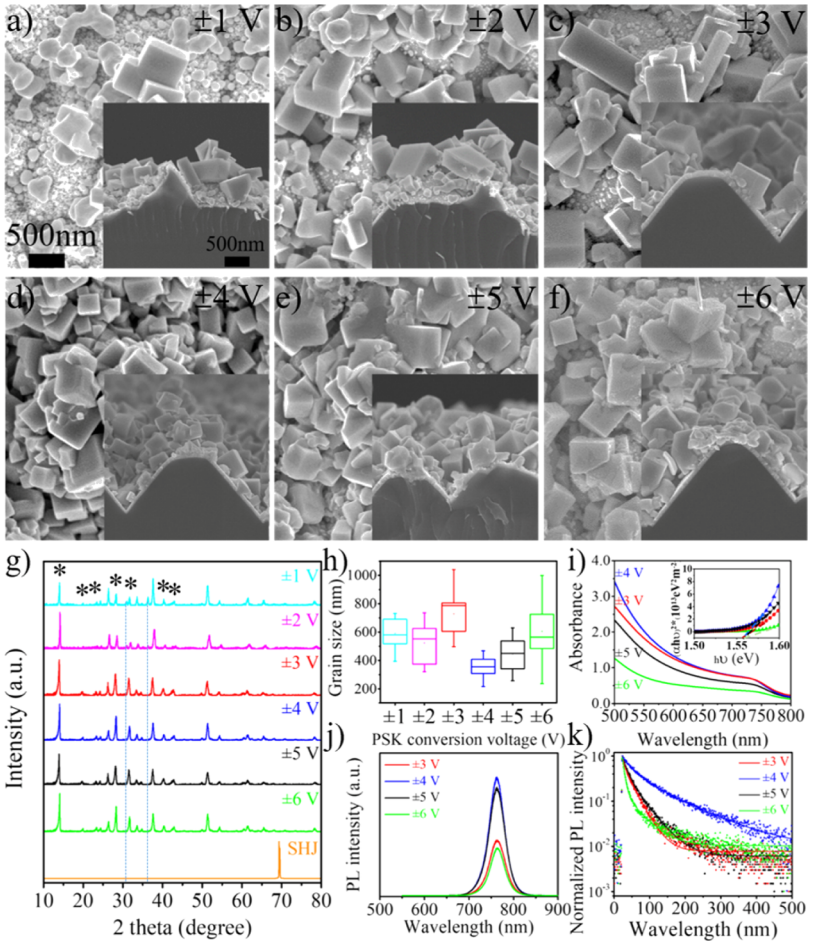

Figure 3. Top-view SEM images of the as-converted PSK on SHJ at symmetric square-wave pulse voltages of (a) ±1, (b) ±2, (c) ±3, (d) ±4, (e) ±5, and (f) ±6 V. The inset images are the corresponding cross-sectional SEM images. (g) XRD patterns of SHJ without and with PSK converted at different pulse voltages. (h) Statistics of the PSK grain sizes at different pulse voltages. (i) UV−vis absorbance of PSK converted at different pulse voltages. The inset is the corresponding Tauc plots. (j) PL and (k) TRPL spectra of PSK converted at different pulse voltages.

of both electrodes.[22] In the SCD model of the electroplating module, there are Butler−Volmer dynamic functions to simulate the deposition of Pb at the cathode and the dissolution of Pb at the anode,[21,22] matching with eqs 1 and 3, respectively.

$$i_{\mathrm{loc,Pb}} = i_{0,\mathrm{Pb}}\left[\exp\left(\frac{\alpha_a F\eta_{\mathrm{Pb}}}{RT}\right) - \exp\left(-\frac{\alpha_c F\eta_{\mathrm{Pb}}}{RT}\right)\right] \quad (6)$$

$$\nu = \frac{i_{\mathrm{loc,Pb}}}{nF}\frac{M}{\rho} \quad (7)$$

$$i_{\mathrm{loc,H}} = -i_{0,\mathrm{H}}10^{-\eta \mathrm{H}/\mathrm{A}_c} \quad (8)$$

First of all, eq 6 defines the local current density ($i_{\mathrm{loc,Pb}}$) of the deposition of Pb at the cathode or dissolution of Pb at the anode, with $i_{0,\mathrm{Pb}}$ as the exchange current density of the Pb reaction. Its value is ∼0.2 A m^{-2}, which can be found in the relevant refs 39 and 40. α_a and α_c are the anode- and cathode-transfer coefficients, which are often set as 0.5 without any special circumstance. F is the Faraday's constant. η is the applied bias voltage. R is the gas constant. T is the thermodynamic temperature, which is 293 K during our experiments. Second, eq 7 represents the speed (ν) of the deposition of Pb at the cathode or the dissolution of Pb at the anode.[39,40] n is the number of participating electrons, which equals 2 in the Pb reaction. M and ρ are the mole mass and density of Pb, respectively. Naturally, the deposition or dissolution thickness of Pb, $d = \nu \cdot t$ (t is the deposition time). Besides, corresponding to eq 2, we need to add a cathode Tafel function to simulate the competitive hydrogen precipitation. Equation 8 defines the local current density ($i_{\mathrm{loc,H}}$) of hydrogen precipitation. $i_{0,\mathrm{H}}$ and A_c are the exchange current density and cathode Tafel gradient of the H reaction, which are 2×10^{-5} A m^{-2} and −118 according to the relevant refs 39 and 40.

Figure 2a′−f′ displays the simulated thickness distribution of the cathode and anode. In the simulation, when we increase the bias voltage, the Pb layer becomes thicker and thicker, which is consistent with the SEM observation in Figure 2a−f. We have drawn the summarized thickness distribution plot in Figure 2g. As seen in Figure 2a−f, the Pb film is a single layer. Therefore, we directly measured the grain sizes and got the average value which equals to the film thickness. The simulated results match well with the measurement. This not only proves that the simulation here is acceptable and believable but also confirms that there is truly an OPD of Pb happening on the pyramid-shaped textured SHJ solar cells with a suitable bias voltage.

We can further take into consideration the anode local current density ($i_{\mathrm{loc,a}}$) and the cathode local current density

https://dx.doi.org/10.1021/acs.jpcc.0c11259
J. Phys. Chem. C 2021, 125, 2875−2883

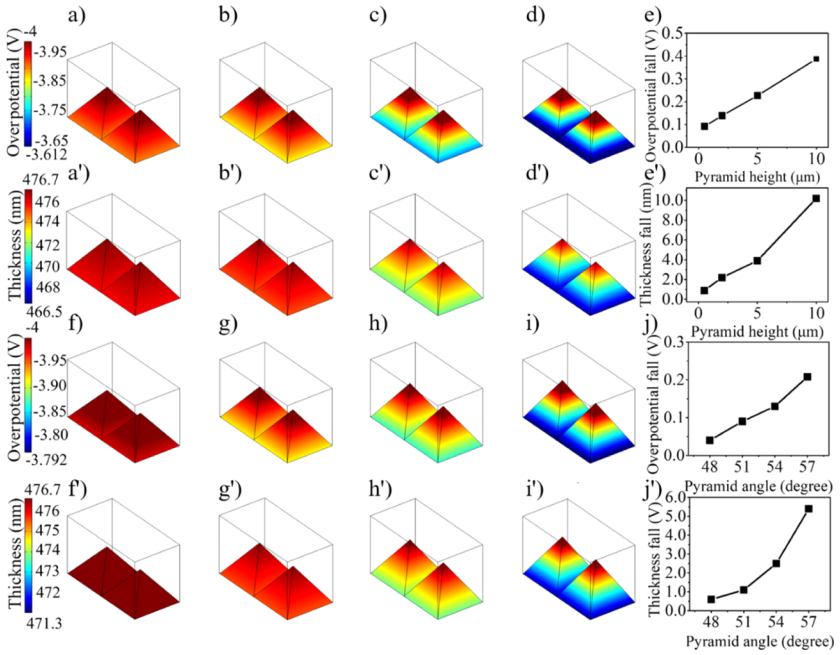

Figure 4. Illustrations of the simulated overpotential distribution on SHJ solar cells with pyramid heights of (a) 500 nm, (b) 2, (c) 5, and (d) 10 μm. (e) Statistics of the simulated overpotential fall on SHJ solar cells with different pyramid heights. Illustrations of the simulated Pb thickness distribution on SHJ solar cells with the pyramid heights of (a′) 500 nm, (b′) 2 μm, (c′) 5 μm, and (d′) 10 μm. (e′) Statistics of the simulated Pb thickness fall on the SHJ solar cells with different pyramid heights. Illustrations of the simulated overpotential distribution on SHJ solar cells with pyramid angles of (f) 48, (g) 51, (h) 54, and (i) 57°. (j) Statistics of the simulated overpotential fall on SHJ solar cells with different pyramid angles. Illustrations of the simulated Pb thickness distribution on SHJ solar cells with pyramid angles of (f′) 48, (g′) 51, (h′) 54, and (i′) 57°. (j′) Statistics of the simulated Pb thickness fall on SHJ solar cells with different pyramid angles.

($i_{loc,c}$) to explain why there are more bubbles generated at higher voltages. Unlike that $i_{loc,a}$ has only one source ($i_{loc,Pb}$), the $i_{loc,c}$ is included with two parts, $i_{loc,Pb}$ and $i_{loc,H}$ (i.e., $i_{loc,c} = i_{loc,Pb} + i_{loc,H}$), matching with the OPD of Pb and hydrogen precipitation, respectively. We define the cathode local current density efficiency ε_c as $i_{loc,Pb}/(i_{loc,Pb} + i_{loc,H})$ [it is obvious that the anode local current density efficiency ε_a always equals 100% ($\varepsilon_a = i_{loc,Pb}/i_{loc,Pb}$)]. We illustrate in Figure 2a″−f″ the relevant simulation results, together with the ε_c values at different potentials in Figure 2i. We can draw the conclusion that ε_c is slightly decreased when we raise the bias voltage from −1 to −4 V. However, it decreased a lot with the bias voltage further raised to −5 and −6 V, which means that the hydrogen precipitation is much stronger at higher voltages. This can explain why there are so many observable bubbles generated at −5 and −6 V bias voltages, where, as shown in Figure 2 e,f, the uniform coverage of Pb on SHJ solar cells is damaged. As a result, the optimized bias voltage is −4 V in step 1 for the electrochemical deposition process of Pb on the pyramid-shaped textured SHJ solar cells.

Conversion of Conformal PSK on SHJ Solar Cells. In step 2, following our precious work,[18] we used a symmetric square-wave pulse voltage to convert Pb into PSK on pyramid-shaped textured SHJ solar cells. We set the amplitude from 1−6 V and the frequency as 5 Hz (i.e., the positive pulse voltage lasts for 100 ms and then the negative pulse voltage for 100 ms in one cycle). Combining the discussion in step 1, we can reveal what exactly happened during the conversion process in step 2. In the positive bias voltage lasting for 100 ms, it is easy to tell that the unit here was a reversed version of the one used in step 1. On the SHJ solar cells with deposited Pb, eq 3 happened, leading to the Pb grains' dissolving into the electrolyte (MAI solution). The yielded Pb^{2+} ions in situ reacted efficiently and fast with MA^+ and I^- ions in the MAI solution as given in eq 9,[18] resulting in the deposition of PSK grains on the SHJ solar cells.

$$Pb^{2+} + MA^+ + 3I^+ \rightarrow MAPbI_3 \quad (9)$$

When the pulse voltage tuned to the negative bias for 100 ms, the Pb^{2+} ions were drifted toward the SHJ solar cells by the strong electric field, that is, more enrichment of Pb^{2+} ions in a smaller distance above the SHJ solar cells.[18] It ensured that the PSK conversion is efficient and continuous.

For convenience, we mark the symmetric square-wave pulse voltage with different amplitudes such as ±1, ±2, ±3, ±4, ±5, and ±6 V, respectively. Figure 3a−f displays the top-view and cross-sectional SEM images of converted PSK on the pyramid-shaped textured SHJ solar cells with different pulse voltage amplitudes. We can find out that when the symmetric square-wave pulse voltage is ±1 and ±2 V, the conversion is incomplete. There are observable Pb grains remaining. Hence, the coverage of PSK on the pyramid-shaped textured SHJ solar cells is not good enough. By raising the pulse voltage amplitude, the Pb grains are fully converted into PSK. At ±4 V pulse voltage, the nanoscale PSK is completely converted and conformably covered on the pyramid-shaped textured SHJ solar cells. However, when the pulse voltage amplitude is higher than 5 V, there are bubbles generated at the surface of the SHJ solar cells during the electrochemical conversion process, which inevitably damages the conformal growth of PSK. The coverage does not satisfy again. The reason why more bubbles are generated at higher amplitudes has been discussed in step 1.

We also conducted an XRD measurement to confirm the existence of PSK with different pulse voltage amplitudes. As we

https://dx.doi.org/10.1021/acs.jpcc.0c11259
J. Phys. Chem. C 2021, 125, 2875−2883

can see in Figure 3g, there are new peaks highlighted with "*" at 14.2, 20.0, 24.6, 28.5, 31.9, 40.6, and 43.2°, corresponding to the [110], [200], [202], [220], [310], [224], and [314] lattice planes of $MAPbI_3$, respectively.[18,27] The other peaks are assigned to ITO as mentioned above. This observation verifies that PSK is successfully converted from Pb with the proposed electrochemistry method on the pyramid-shaped textured SHJ solar cells. However, we also need to point out that in the XRD patterns of ±1 and ±2 V, there are still two peaks at 31.4 and 36.4°, which are assigned to the [111] and [200] crystal planes of lead, respectively. This proves that there are residual Pb grains on SHJ solar cells, consistent with the SEM observation. We further illustrate the statistics of PSK grain sizes in Figure 3h, where the average size equals the film thickness. We can draw the conclusion that at the pulse voltage of ±4 V, not only the PSK grain size distribution is much more concentrated, but also the shape-preserving growth of the nanoscale PSK can be realized on pyramid-shaped textured SHJ solar cells (also see Figure 3a–f).

After the morphology and structure analysis, we move forward to study the optical properties of the as-converted PSK. For clearance, we did not investigate the samples under pulse voltages of ±1 and ±2 V due to the incomplete conversion. The UV–vis absorption and relevant Tauc plots are shown in Figure 3i. We can notice that the PSK converted at ±4 V exhibits the strongest absorption of the visible light among all the samples, and the absorption edges do not shift in spite of different pulse voltage amplitudes. It conforms to the common PSK optical band energy of 1.56 eV.[41] The PL and TRPL spectra are shown in Figure 3j,k, respectively. The stronger luminescence intensity than others indicates that there are least defects[18] in the ±4 V sample. That is crucial to the generation and transportation of charge carriers in PSK. Accordingly, the longest fluorescence lifetime is expected there for the most efficient charge-carrier transportation. Apparently, both the PL and TRPL results are in good agreement with the UV–vis absorption observation, revealing the best optical properties achieved in the PSK converted at ±4 V. The above results demonstrate clearly that the proposed two-step electrochemical deposition method is achievable and efficient for the conformal growth of nanoscale PSK on pyramid-shaped textured SHJ solar cells.

Theoretical Investigation on the Pyramid Height and Angle Dependence. In the preceding discussion about the morphology of either Pb or PSK, we notice that the obtained grains at the top end of pyramids are always a bit larger than those at the base (as shown in Figures 2a–f and 3a–f). In other words, the thickness distribution along the pyramids is nonuniform other than idealized homogeneous. Apparently, it will not happen on the flat substrate, for example, FTO glass.[16,18] We attribute this phenomenon to the inevitable nonuniform overpotential distribution along the pyramids, which is originally induced by the micrometer-level up-and-down pyramid shape of the textured SHJ solar cells. Therefore, we further investigated theoretically the influence of the pyramid heights and angles on the overpotential and Pb (as well as PSK) thickness distribution.

Figure 4a–d and a′–d′ displays the relevant simulation results of the overpotential and Pb thickness distribution along the pyramids of different heights. We set the pyramid heights at 500 nm, 2 μm (which is employed in the former discussions), 5, and 10 μm, respectively, under the pyramid angle at 51° and the optimized applied bias voltage of −4 V. We have drawn the summarized plots of the overpotential and Pb thickness fall between the top end and the base of the pyramid in Figure 4e and e′, respectively. We can conclude that when we increase the height of pyramids from 500 nm to 10 μm, the overpotential distribution becomes more and more dispersed. Accordingly, the overpotential fall between the top end and the base of the pyramid increases from 0.092 to 0.388 V. Consequently, the uniformity of the Pb thickness distribution is damaged by the increased pyramid heights due to the dispersed overpotential distribution. The Pb thickness fall between the top end and the base of the pyramid increased from 0.9 to 10.2 nm, which is according to the fact that the obtained grains at the top end of pyramids are always a bit larger than those at the base. Definitely, the nonuniformly deposited Pb grains will lead to the nonuniformly converted PSK grains on the pyramid-shaped textured SHJ solar cells (as we can see in Figure 3a–f). Hence, if we would like to obtain uniform PSK layers on pyramid-shaped textured SHJ solar cells, we should lower the pyramid heights as much as we can. However, there are economic efficiency issues to be considered[1] in the industrial manufacture of SHJ solar cells. We can conclude that the 2 μm pyramid height is the best solution on pyramid-shaped textured SHJ solar cells combining the experimental feasibility and small Pb thickness fall of 2.2 nm.

Finally, we move forward to the pyramid angle impact. Figure 4f–i, f′–i′ illustrates the corresponding simulation results of the overpotential and Pb thickness distribution along the pyramids of different angles. We set the pyramid angle at 48, 51° (which is used in the former discussions), 54, and 57°, respectively. The pyramid height is 2 μm and the applied bias voltage is also −4 V. We also summarized the overpotential and Pb thickness fall between the top end and the base of the pyramid in Figure 4j,j′, respectively. We can find out that with the pyramid angle increasing from 48 to 57°, the overpotential distribution becomes more and more dispersed as in the case of pyramid heights. The overpotential fall between the top end and the base of the pyramid increased from 0.04 to 0.208 V. As a result, the Pb thickness fall increased from 0.6 to 5.4 nm, which will certainly lead to the nonideally converted PSK layer on the pyramid-shaped textured SHJ solar cells (as we can see in Figure 3a–f). It tells us that in order to realize the uniform coverage of the PSK layer on the pyramid-shaped textured SHJ solar cells, we should lower the pyramid angles as much as we can. However, we cannot ignore the light trap requirements for high-performance solar cells.[37] If the angles were too low, the light trap function of the pyramids would fail. Therefore, we need to accept the 51° pyramid angle solution to meet the industrial reality, especially considering the fact that the Pb thickness fall is only 0.5 nm larger than the case of the 48° pyramid angle.

CONCLUSIONS

To solve the process complexity and the high cost of existing methods for preparing PSK on textured c-Si solar cells, we have introduced a simple and manageable two-step electrochemical deposition scheme to successfully deposit shape-preserving and nanoscale PSK on the traditional pyramid-shaped textured SHJ solar cells. The Pb deposition and PSK conversion can be conveniently optimized by adjusting the bias voltage, and the entire electrochemical deposition process can be completed in a few minutes. Combining the simulation based on the Butler–Volmer model, we have verified that there are simultaneous

https://dx.doi.org/10.1021/acs.jpcc.0c11259
J. Phys. Chem. C 2021, 125, 2875–2883

OPD of Pb and hydrogen precipitation during the electrochemical process. The latter becomes stronger at higher voltages, leading to unsatisfied Pb deposition and PSK conversion. The theoretical investigation on the influence of the pyramid height and angle further reveals the existence of nonuniform overpotential determining the Pb deposition and PSK conversion. Our research provides a new way toward efficient and low-cost PSK/c-Si monolithic TSCs.

AUTHOR INFORMATION

Corresponding Author

Wenzhong Shen − *Key Laboratory of Artificial Structures and Quantum Control (Ministry of Education), Institute of Solar Energy, School of Physics and Astronomy, Shanghai Jiao Tong University, Shanghai 200240, China*; Email: wzshen@sjtu.du.cn

Authors

Yangrunqian Wang − *Key Laboratory of Artificial Structures and Quantum Control (Ministry of Education), Institute of Solar Energy, School of Physics and Astronomy, Shanghai Jiao Tong University, Shanghai 200240, China*; orcid.org/0000-0003-4746-2360

Chao Gao − *Key Laboratory of Artificial Structures and Quantum Control (Ministry of Education), Institute of Solar Energy, School of Physics and Astronomy, Shanghai Jiao Tong University, Shanghai 200240, China*

Xin Wang − *Key Laboratory of Artificial Structures and Quantum Control (Ministry of Education), Institute of Solar Energy, School of Physics and Astronomy, Shanghai Jiao Tong University, Shanghai 200240, China*

Hong Liu − *Key Laboratory of Artificial Structures and Quantum Control (Ministry of Education), Institute of Solar Energy, School of Physics and Astronomy, Shanghai Jiao Tong University, Shanghai 200240, China*; orcid.org/0000-0002-2241-1199

Complete contact information is available at: https://pubs.acs.org/10.1021/acs.jpcc.0c11259

Notes

The authors declare no competing financial interest.

ACKNOWLEDGMENTS

This work was supported by the National Natural Science Foundation of China (11834011, 11974242). We would like to thank the Advanced Electronic Materials and Devices (AEMD) of the Shanghai Jiao Tong University for supplying the facility of scanning electron microscopy (SEM). We appreciate the help with software COMSOL Multiphysics by Dr. Zhiwen Shi from the School of Physics, Shanghai Jiao Tong University.

ABBREVIATIONS

PSK	perovskite
c-Si	crystalline silicon
TSCs	tandem solar cells
PCE	power conversion efficiency
IZO	indium zinc oxide
ITO	indium tin oxide
PDMS	polydimethylsiloxane
SHJ	silicon heterojunction
OPD	overpotential deposition
UPD	underpotential deposition
XRD	X-ray diffraction
TCOs	transparent conducting oxides
PL	photoluminescence
TRPL	time-resolved photoluminescence
FESEM	field-emission scanning electron microscopy

REFERENCES

(1) Battaglia, C.; Cuevas, A.; De Wolf, S. High-efficiency crystalline silicon solar cells: status and perspectives. *Energy Environ. Sci.* **2016**, *9*, 1552−1576.

(2) Best Research-Cell Efficiency Chart. https://www.nrel.gov/pv/assets/pdfs/best-research-cell-efficiencies.20200104.pdf (accessed Dec 18, 2020).

(3) Shockley, W.; Queisser, H. J. Detailed Balance Limit of Efficiency of p-n Junction Solar Cells. *J. Appl. Phys.* **1961**, *32*, 510−519.

(4) Yu, Z.; Leilaeioun, M.; Holman, Z. Selecting tandem partners for silicon solar cells. *Nat. Energy* **2016**, *1*, 16137.

(5) Mailoa, J. P.; Bailie, C. D.; Johlin, E. C.; Hoke, E. T.; Akey, A. J.; Nguyen, W. H.; McGehee, M. D.; Buonassisi, T. A 2-terminal perovskite/silicon multijunction solar cell enabled by a silicon tunnel junction. *Appl. Phys. Lett.* **2015**, *106*, 121105.

(6) Albrecht, S.; Saliba, M.; Correa Baena, J. P.; Lang, F.; Kegelmann, L.; Mews, M.; Steier, L.; Abate, A.; Rappich, J.; Korte, L.; et al. Monolithic perovskite/silicon-heterojunction tandem solar cells processed at low temperature. *Energy Environ. Sci.* **2016**, *9*, 81−88.

(7) Werner, J.; Weng, C.-H.; Walter, A.; Fesquet, L.; Seif, J. P.; De Wolf, S.; Niesen, B.; Ballif, C. Efficient Monolithic Perovskite/Silicon Tandem Solar Cell with Cell Area >1 cm^2. *J. Phys. Chem. Lett.* **2016**, *7*, 161−166.

(8) Bush, K. A.; Palmstrom, A. F.; Yu, Z. J.; Boccard, M.; Cheacharoen, R.; Mailoa, J.; McMeekin, D.; Hoye, R.; Bailie, C.; Leijtens, T.; et al. 23.6%-efficient monolithic perovskite/silicon tandem solar cells with improved stability. *Nat. Energy* **2017**, *2*, 17009.

(9) Werner, J.; Niesen, B.; Ballif, C. Perovskite/Silicon Tandem Solar Cells: Marriage of Convenience or True Love Story?−An Overview. *Adv. Mater. Interfaces* **2018**, *5*, 1700731.

(10) Hou, Y.; Aydin, E.; De Bastiani, M.; Xiao, C.; Isikgor, F. H.; Xue, D.-J.; Chen, B.; Chen, H.; Bahrami, B.; Chowdhury, A. H.; et al. Efficient tandem solar cells with solution-processed perovskite on textured crystalline silicon. *Science* **2020**, *367*, 1135.

(11) Sahli, F.; Werner, J.; Kamino, B. A.; Bräuninger, M.; Monnard, R.; Paviet-Salomon, B.; Barraud, L.; Ding, L.; Diaz Leon, J. J.; Sacchetto, D.; et al. Fully textured monolithic perovskite/silicon tandem solar cells with 25.2% power conversion efficiency. *Nat. Mater.* **2018**, *17*, 820.

(12) Chen, B.; Yu, Z. J.; Manzoor, S.; Wang, S.; Weigand, W.; Yu, Z.; Yang, G.; Ni, Z.; Dai, X.; Holman, Z. C.; et al. Blade-Coated Perovskites on Textured Silicon for 26%-Efficient Monolithic Perovskite/Silicon Tandem Solar Cells. *Joule* **2020**, *4*, 850−864.

(13) Lamanna, E.; Matteocci, F.; Calabro, E.; Serenelli, L.; Salza, E.; Martini, L.; Menchini, F.; Izzi, M.; Agresti, A.; Pescetelli, S.; et al. Mechanically Stacked, Two-Terminal Graphene-Based Perovskite/Silicon Tandem Solar Cell with Efficiency over 26%. *Joule* **2020**, *4*, 865−881.

(14) Rashkova, B.; Guel, B.; Pötzschke, R. T.; Staikov, G.; Lorenz, W. J. Electrodeposition of Pb on n-Si(111). *Electrochim. Acta* **1998**, *43*, 3021−3028.

(15) Huang, J.-h.; Jiang, K.-j.; Cui, X.-p.; Zhang, Q.-q.; Gao, M.; Su, M.-j.; Yang, L.-m.; Song, Y. Direct Conversion of $CH_3NH_3PbI_3$ from Electrodeposited PbO for Highly Efficient Planar Perovskite Solar Cells. *Sci. Rep.* **2015**, *5*, 15889.

(16) Cui, X.-P.; Jiang, K.-J.; Huang, J.-H.; Zhou, X.-Q.; Su, M.-J.; Li, S.-G.; Zhang, Q.-Q.; Yang, L.-M.; Song, Y.-L. Electrodeposition of PbO and its in situ conversion to $CH_3NH_3PbI_3$ for mesoscopic perovskite solar cells. *Chem. Commun.* **2015**, *51*, 1457−1460.

(17) Chen, H.; Wei, Z.; Zheng, X.; Yang, S. A scalable electrodeposition route to the low-cost, versatile and controllable fabrication of perovskite solar cells. *Nano Energy* **2015**, *15*, 216−226.
(18) Zhou, F.; Liu, H.; Wang, X.; Shen, W. Fast and Controllable Electric-Field-Assisted Reactive Deposited Stable and Annealing-Free Perovskite toward Applicable High-Performance Solar Cells. *Adv. Funct. Mater.* **2017**, *27*, 1606156.
(19) *Proceedings of the 25th European Photovoltaic Solar Energy Conference and Exhibition and the 5th World Conference on Photovoltaic Energy Conversion*; 2010.
(20) Conway, B. E., *Theory and Principles of Electrode Process*; Ronald: New York, 1965; Chapter 6.
(21) Bockris, J. O.-'M., Reddy, A. K. N. *Modern Electrochemistry*; Plenum: New York, 1970; *Vol. 2*, Chapter 8.
(22) Erdey-Gruz, T., *Kinetics of Electrode Processes*; Wiley-Interscience: New York, 1972; Chapter 1.
(23) Butler, J. A. V. Studies in heterogeneous equilibria. Part II.—The kinetic interpretation of the nernst theory of electromotive force. *Trans. Faraday Soc.* **1924**, *19*, 729−733.
(24) Erdey-Grúz, T.; Volmer, M. Zur Theorie der Wasserstoff Überspannung. *Z. Phys. Chem., Abt. A.* **1930**, *150*, 203−213.
(25) Yang, L.; Zhong, S.; Zhang, W.; Li, X.; Li, Z.; Zhuang, Y.; Wang, X.; Zhao, L.; Cao, X.; Deng, X.; et al. Study and development of rear-emitter Si heterojunction solar cells and application of direct copper metallization. *Prog. Photovoltaics* **2018**, *26*, 385−396.
(26) Kojima, A.; Teshima, K.; Shirai, Y.; Miyasaka, T. Organometal Halide Perovskites as Visible-Light Sensitizers for Photovoltaic Cells. *J. Am. Chem. Soc.* **2009**, *131*, 6050−6051.
(27) Burschka, J.; Pellet, N.; Moon, S.-J.; Humphry-Baker, R.; Gao, P.; Nazeeruddin, M. K.; Grätzel, M. Sequential deposition as a route to high-performance perovskite-sensitized solar cells. *Nature* **2013**, *499*, 316−319.
(28) Li, F.; Pei, Y.; Xiao, F.; Zeng, T.; Yang, Z.; Xu, J.; Sun, J.; Peng, B.; Liu, M. Tailored dimensionality to regulate the phase stability of inorganic cesium lead iodide perovskites. *Nanoscale* **2018**, *10*, 6318−6322.
(29) Li, F.; Xie, Y.; Hu, Y.; Long, M.; Zhang, Y.; Xu, J.; Qin, M.; Lu, X.; Liu, M. Effects of Alkyl Chain Length on Crystal Growth and Oxidation Process of Two-Dimensional Tin Halide Perovskites. *ACS Energy Lett.* **2020**, *5*, 1422−1429.
(30) Wang, Y.; Li, J.; Li, Q.; Zhu, W.; Yu, T.; Chen, X.; Yin, L. a.; Zhou, Y.; Wang, X.; Zou, Z. PbI_2 heterogeneous-cap-induced crystallization for an efficient $CH_3NH_3PbI_3$ layer in perovskite solar cells. *Chem. Commun.* **2017**, *53*, 5032−5035.
(31) Meites, L., *Polarographic Techniques*, 2nd ed.; Wiley-Interscience, 1965.
(32) Horváth, O.; Mikó, I. Spectra, equilibrium and photoredox chemistry of tri- and tetraiodoplumbate(II) complexes in acetonitrile. *J. Photochem. Photobiol., A* **1998**, *114*, 95−101.
(33) Takahashi, S.; Aramata, A.; Nakamura, M.; Hasebe, K.; Taniguchi, M.; Taguchi, S.; Yamagishi, A. Electrochemical and in situ STM studies of anomalous phosphate adsorption induced on Zn UPD at Au(111) in the presence of halide ions in aqueous phosphate solutions. *Surf. Sci.* **2002**, *512*, 37−47.
(34) Mendoza-Huizar, L. H.; Robles, J.; Palomar-Pardavé, M. Nucleation and growth of cobalt onto different substrates Part II. The upd-opd transition onto a gold electrode. *J. Electroanal. Chem.* **2003**, *545*, 39−45.
(35) Wu, G. Y.; Bae, S.-E.; Gewirth, A. A.; Gray, J.; Zhu, X. D.; Moffat, T. P.; Schwarzacher, W. Pb electrodeposition on polycrystalline Cu in the presence and absence of Cl-: A combined oblique incidence reflectivity difference and in situ AFM study. *Surf. Sci.* **2007**, *601*, 1886−1891.
(36) Lai, Y.; Liu, F.; Li, J.; Zhang, Z.; Liu, Y. Nucleation and growth of selenium electrodeposition onto tin oxide electrode. *J. Electroanal. Chem.* **2010**, *639*, 187−192.
(37) Taguchi, M.; Kawamoto, K.; Tsuge, S.; Baba, T.; Sakata, H.; Morizane, M.; Uchihashi, K.; Nakamura, N.; Kiyama, S.; Oota, O. HITTM cells—high-efficiency crystalline Si cells with novel structure. *Prog. Photovoltaics* **2000**, *8*, 503−513.
(38) Kim, N.-K.; Min, Y.; Noh, S.; Cho, E.; Jeong, G.; Joo, M.; Ahn, S.-W.; Lee, J.; Kim, S.; Ihm, K.; et al. Investigation of Thermally Induced Degradation in $CH_3NH_3PbI_3$ Perovskite Solar Cells using In-situ Synchrotron Radiation Analysis. *Sci. Rep.* **2017**, *7*, 4645−4653.
(39) Bard, A. J. *Encyclopedia of Electrochemistry of the Elements*; Marcel Dekker: New York, 1973, p 1980.
(40) NIST-JANAF Thermochemical Tables. https://janaf.nist.gov/ (accessed Dec 18, 2020).
(41) De Wolf, S.; Holovsky, J.; Moon, S.-J.; Löper, P.; Niesen, B.; Ledinsky, M.; Haug, F.-J.; Yum, J.-H.; Ballif, C. Organometallic Halide Perovskites: Sharp Optical Absorption Edge and Its Relation to Photovoltaic Performance. *J. Phys. Chem. Lett.* **2014**, *5*, 1035−1039.

https://dx.doi.org/10.1021/acs.jpcc.0c11259
J. Phys. Chem. C 2021, 125, 2875−2883